Fe-H melting curve below 3 GPa: Implications for hydrogen in the lunar core

J. Takeshita, K. Hirose, S. Fu, F. Sakai, K. Hikosaka

Supplementary Information

The Supplementary Information includes:

- Experimental Methods
- Estimates of the Hydrogen Content in Liquid Iron
- Calculations of Metal-Silicate Partitioning of Hydrogen
- Tables S-1 and S-2
- Figures S-1 to S-4
- Supplementary Information References

Experimental Methods

High-pressure and -temperature (*P-T*) experiments were conducted in a laser-heated diamond-anvil cell (LH-DAC) using diamond anvils with flat 800 μm culet (we can precisely control experimental pressure by using anvils with such large culet size). The anvil surface was coated with a 500 nm-thick Ti layer by sputtering in order to prevent hydrogen penetration into diamonds (Ohta *et al.*, 2015). We loaded a pure Fe foil (Toho Zinc, >99.999% purity) with a thickness of approximately 20 μm into a hole at the centre of a pre-indented Re gasket, leaving space for hydrogen. Pressure markers of KCl and a ruby ball were placed beneath the Fe foil. Subsequently the DAC was placed in an oven maintained at 120 °C for 1 hour in order to remove moisture from the KCl. Supercritical hydrogen fluid was introduced into the sample chamber using a high-pressure gas apparatus (PRETECH Co., Ltd) at SPring-8. The high-pressure vessel and gas line were evacuated for 5 minutes and subsequently purged four times with H_2 gas prior to loading into the DAC. The presence of H_2 molecules was confirmed by Raman spectra. The sample was then compressed to a target pressure, with monitoring pressure by the ruby ball.

We obtained X-ray diffraction (XRD) data at the beamline BL10XU of SPring-8. The incident X-ray beam was monochromatized to ~30 keV and focused to 6 μm in diameter (full-width at half maximum). XRD patterns were collected using a flat panel X-ray detector (Varex Imaging, XRD1611CP3). The obtained 2D XRD images were converted into 1D patterns using IPAnalyzer software (Seto *et al.*, 2010), and phase identification and unit-cell volume derivation were performed. We heated the Fe + H_2 sample from both sides

using a couple of 100 W single-mode Yb fibre lasers (SPI Lasers Co. Ltd.). The laser spot size was approximately 50 μm in diameter. Using visible fluorescence that appeared upon irradiating X-ray onto the KCl medium, the laser beams from both sides were adjusted to be coaxial with the X-ray beam. The laser power output was increased stepwise, and the XRD spectrum and temperature were collected/measured each time. The laser power output was maintained for several tens of seconds at each step. We measured temperature at the iron sample surface by a spectro-radiometric method (Hirao *et al.*, 2020). The average within the 6 μm area probed by the XRD beam was adopted as the sample temperature. While Mita *et al.* (2025) considered 5% uncertainty for both the upper and lower bounds, we employed a much thicker (20 μm) iron sample in this study, which causes larger temperature variations in axial direction toward the sample inside (hottest at the surface and colder inside). The earlier laser-heated DAC experiments by Tateno *et al.* (2018) demonstrated an axial temperature gradient of about 18 K/μm in their 9.4 μm thick Fe sample (see their Fig. 1b), which corresponds to 0.7–0.8% of the surface temperature (2350 K) per μm. We therefore consider additional −7% (total −12% for the lower bound) temperature variations from the surface to the core (centre) in our sample. Pressure under high temperature was determined from the lattice volume of the B1 or B2 phase of KCl and their thermal equations of state (EoSs, Walker *et al.*, 2002; Tateno *et al.*, 2019). The pressure error was evaluated by considering uncertainties in the lattice volume and temperature of the KCl pressure marker, which was in contact with a diamond anvil on one side and covered with hydrogen on the other side. We consider that the temperature of the KCl ranged from 300 K to an effective temperature that is given by Campbell *et al.* (2009) as $(3 \times T_{\mathrm{measured}} + 300) / 4$, in which T_{measured} represents the measured iron sample temperature (or the melting temperature of KCl, whichever was lower). The resulting pressure uncertainty was dominated by the uncertainty in the estimated KCl temperature.

It is known that hydrogen escapes from iron when it turns to the bcc phase (*e.g.,* Iizuka-Oku *et al.*, 2017; Tagawa *et al.*, 2021). It is necessary to determine hydrogen concentration x in fcc FeH_x at high P-T because it transforms into the bcc phase upon quenching temperature in the pressure range of the present experiments. The hydrogen content is calculated as:

$$x = \frac{V_{\mathrm{FeH}_x} - V_{\mathrm{Fe}}}{\Delta V_{\mathrm{H}}} \tag{S-1}$$

where V represents the volume per chemical formula (half of the unit-cell volume of fcc). V_{Fe} for the fcc phase was derived from the EoS of pure fcc-Fe reported by Tsujino *et al.* (2013). ΔV_{H} (= 2.22 Å^3), the volume expansion upon incorporation of one hydrogen atom into the Fe lattice, was adopted from the value for fcc FeH_x at 4–12 GPa and about 1000 K reported by Ikuta *et al.* (2019).

Estimates of the Hydrogen Content in Liquid Iron

The amount of hydrogen in liquid iron could not be obtained in the manner described above, because the liquids crystallized into bcc Fe upon quenching temperature, which does not incorporate hydrogen into its lattice. Alternatively, we obtained the density of liquid FeH_x and then determined x considering ΔV_{H}. First, liquid density was calculated from the diffuse scattering signal in XRD data by non-iterative extension procedures described by Kuwayama *et al.* (2020), which were built on earlier diffuse-scattering analyses for liquid density determination, including Eggert *et al.* (2002) (Fig. S-4). High-pressure XRD measurements in a DAC always have a limitation on the range of momentum transfer Q (up to Q_{max}) because of a geometrical constraint, which leads to artificial oscillations in distribution function $F(r)$ and pair distribution function $g(r)$. Indeed, no atoms can exist at distances shorter than the nearest-neighbour atomic distance ($r < r_{\mathrm{min}}$), meaning that the local density must be zero. We therefore complemented the data to satisfy such physical requirement, $g(r) = 0$ at $r < r_{\mathrm{min}}$ (in other words, for $F(r)$ to exhibit a straight line with a slope of $-4\pi\rho r$, where ρ is the average atomic number density). In this procedure, only the unmeasured high-Q part beyond Q_{max} was supplemented.

For each liquid density measurement, an XRD pattern collected immediately below the melting temperature at the same sample position was used as the background. The liquid diffuse scattering signal was obtained as:

$$I_{\mathrm{liq}}(Q) = I_{\mathrm{melt}}(Q) - sI_{\mathrm{bk}}(Q) \quad \text{(S-2)}$$

where $I_{\mathrm{melt}}(Q)$ and $I_{\mathrm{bk}}(Q)$ are the XRD patterns collected above and below the melting temperature, respectively, and s is a scale factor accounting for small differences in the incident X-ray intensity and background level. Note that both patterns were collected through the identical diamond anvils and along the same X-ray path. Therefore, subtracting the unmelted pattern from the melting pattern should largely remove scattering contributions common to both measurements, including Compton scattering from the diamonds. The resulting diffuse intensity was then normalized using the composition-dependent factor of the FeH_x liquid, $\langle f \rangle$. Because hydrogen contributes negligibly to the X-ray scattering signal, $\langle f \rangle$ was approximated by the Fe atomic form factor, $f_{\mathrm{Fe}(Q)}$. Subsequently $S(Q)$ of liquid Fe-H is calculated as:

$$S(Q) = \frac{\alpha_{\mathrm{N}} I(Q)}{f^2_{\mathrm{Fe}(Q)}} \quad \text{(S-3)}$$

where α_{N} is a normalization factor.

The density was determined by searching for a parameter set that minimizes the deviation of $g(r)$ from zero at $r < r_{\mathrm{min}}$. In the fitting, r_{min}, the scale factor s, normalization factor α_{N}, density ρ, and Q_{max} were allowed to vary together. The derived density typically includes ±~2% uncertainty. More technical details are found in Kuwayama *et al.* (2020) and Fu *et al.* (2025), who derived the densities of liquids Fe and FeH_x, respectively. The hydrogen content in liquid FeH_x is then estimated from the density difference from liquid pure Fe using $\Delta V_{\mathrm{H}} = 2.22$ Å^3 from Ikuta *et al.* (2019). The density of liquid Fe is from the EoS by Kuwayama *et al.* (2020). Although the liquid density measurements by Kuwayama *et al.* (2020) were conducted at 21.5 GPa and higher pressures, their EoS well reproduces the known density of liquid Fe at 1 bar and its sound velocity data below 5.8 GPa, despite these low-pressure data not being used in obtaining their EoS. According to the EoSs of liquid Fe by Kuwayama *et al.* (2020) and liquid Fe-H by Fu *et al.* (2025), the densities of Fe and $FeH_{0.3}$ are 7.47 and 7.13 g/cm^3, respectively, at 5 GPa and 1700 K, indicating $\Delta V_{\mathrm{H}} = 2.17$ Å^3, which matches the value by Ikuta *et al.* (2019). The uncertainty in x was calculated by first-order propagation of the uncertainties in pressure, temperature, Fe number density, and ΔV_{H}.

Calculations of Metal-Silicate Partitioning of Hydrogen

The hydrogen content in the lunar core was calculated using $D_{\mathrm{H}}^{\mathrm{metal/silicate}}$ (molar basis) reported by Tsutsumi *et al.* (2025). We adopted the lunar primitive upper mantle composition from Longhi (2003) for the LMO composition and 0 to 7 wt. % S in the core following Jing *et al.* (2014). Note that Tsutsumi *et al.* (2025)'s $D_{\mathrm{H}}^{\mathrm{metal/silicate}}$ values were obtained by considering that hydrogen does not have a colligative property in iron solvent since small H atoms are incorporated into liquid Fe interstitially and therefore the activity of element i in metal is approximated as:

$$x_i' = \frac{N_i}{\sum_{k \neq \mathrm{H}} N_k} \quad \text{(S-4)}$$

Supplementary Tables

Table S-1 Experimental results on melting and hydrogen content x in FeH_x.

Run		#1		#2	
Spot		#1-1	#1-2	#2-1	#2-2
Subsolidus	P [GPa]	1.3(4)	1.0(4)	2.1(4)	3.0(3)
	T [K]	$1490(^{+70}_{-180})$	$1590(^{+80}_{-190})$	$1360(^{+70}_{-160})$	$1230(^{+60}_{-150})$
Right above solidus	P [GPa]	1.5(5)	1.0(4)	2.2(4)	3.3(4)
	T [K]	$1530(^{+80}_{-180})$	$1640(^{+80}_{-200})$	$1440(^{+70}_{-170})$	$1380(^{+70}_{-170})$
	x (fcc)	0.16(5)	0.08(6)	0.22(5)	0.29(4)
Liquid density measurements	P [GPa]	–	1.0(4)	2.2(4)	3.6(4)
	T [K]	–	$1710(^{+90}_{-210})$	$1530(^{+80}_{-180})$	$1670(^{+80}_{-200})$
	ρ (liquid) [g/cm^3]	–	7.03(12)	7.12(14)	6.87(12)
	x (liquid)	–	$0.14(^{+16}_{-13})$	$0.20(^{+14}_{-13})$	$0.48(^{+17}_{-15})$

Table S-2 Partitioning of H under representative core-formation conditions and resulting its abundance in the lunar core.

Pressure (GPa)	Temperature (K)	$D_H^{metal/silicate}$	Core H (wt. %) for LMO H_2O = 300 µg/g	Core H (wt. %) for LMO H_2O = 1000 µg/g
2.8	2163	1.11×10^2	0.3	1.1
5.0	2200	1.05×10^2	0.3	1.1
5.0	3200	1.85×10^2	0.6	1.8

Supplementary Figures

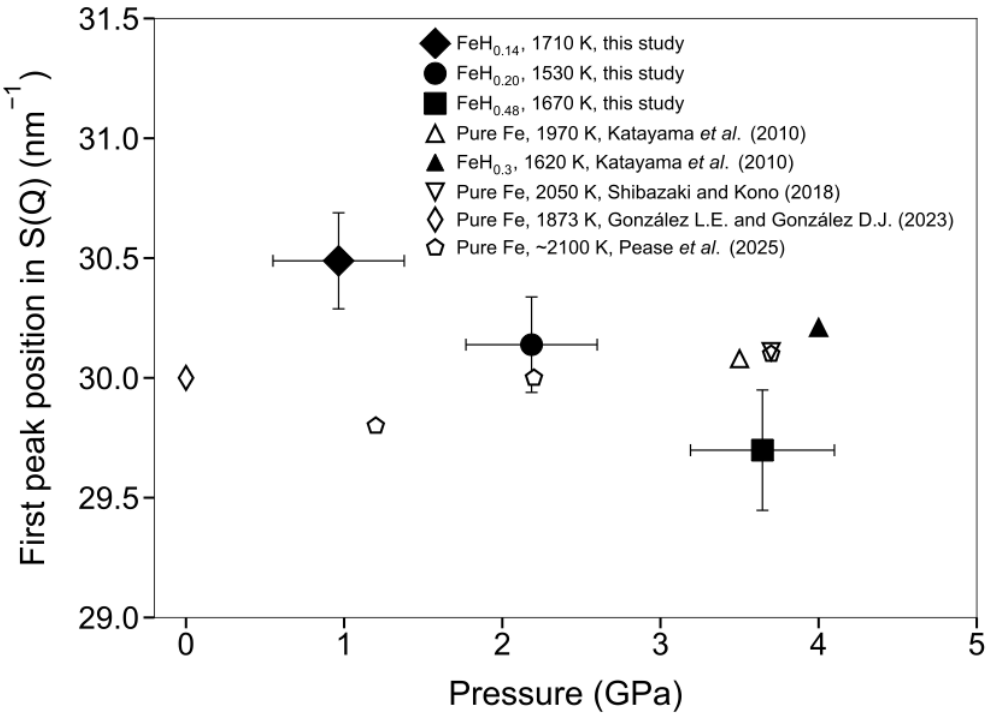

Figure S-1 The first peak position in the structure factor $S(Q)$. The observed shift for liquid FeH_x indicates a larger volume and thus higher hydrogen concentration with increasing pressure from 1.0 to 3.6 GPa. Note that the $S(Q)$ profile of this study is merely the one for the purpose of yielding the correct $g(r)$ and $F(r)$ (see Fig. S-4).

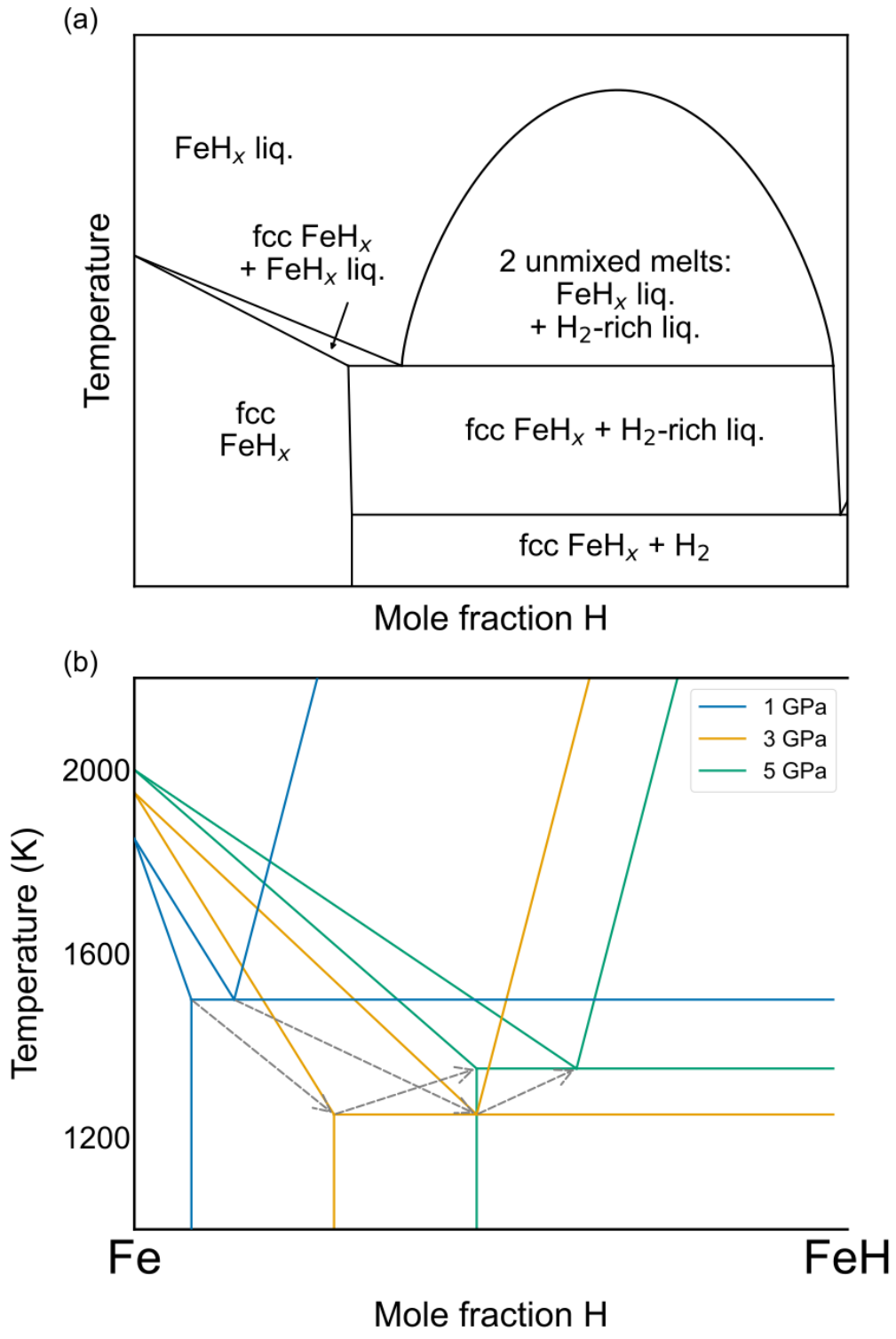

Figure S-2 **(a)** Schematic phase diagram between Fe and H_2 under pressure (less than ~10 GPa) based on Tagawa *et al.* (2022) and Stoutenburg *et al.* (2026). **(b)** The Fe-rich portion of the Fe-H phase diagram, showing the enhanced solubilities of hydrogen in solid and liquid iron and the changes in solidus temperature with increasing pressure from 1 to 5 GPa.

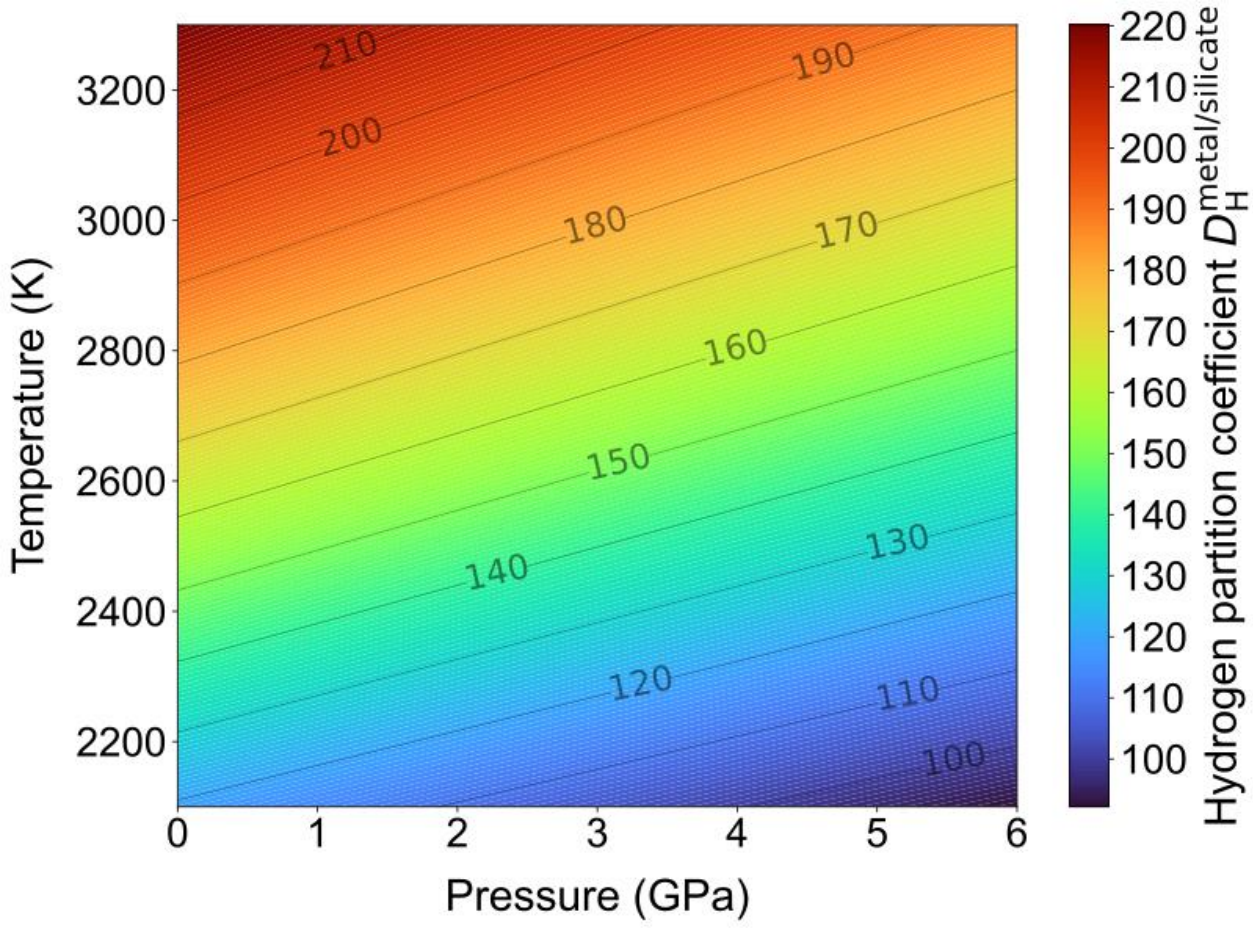

Figure S-3 Metal-silicate partition coefficient of hydrogen ($D_H^{metal/silicate}$, molar basis) as functions of pressure and temperature from Tsutsumi *et al.* (2025), considering ΔIW = −2 (Rai and van Westrenen, 2014) and carbon-free metal composition.

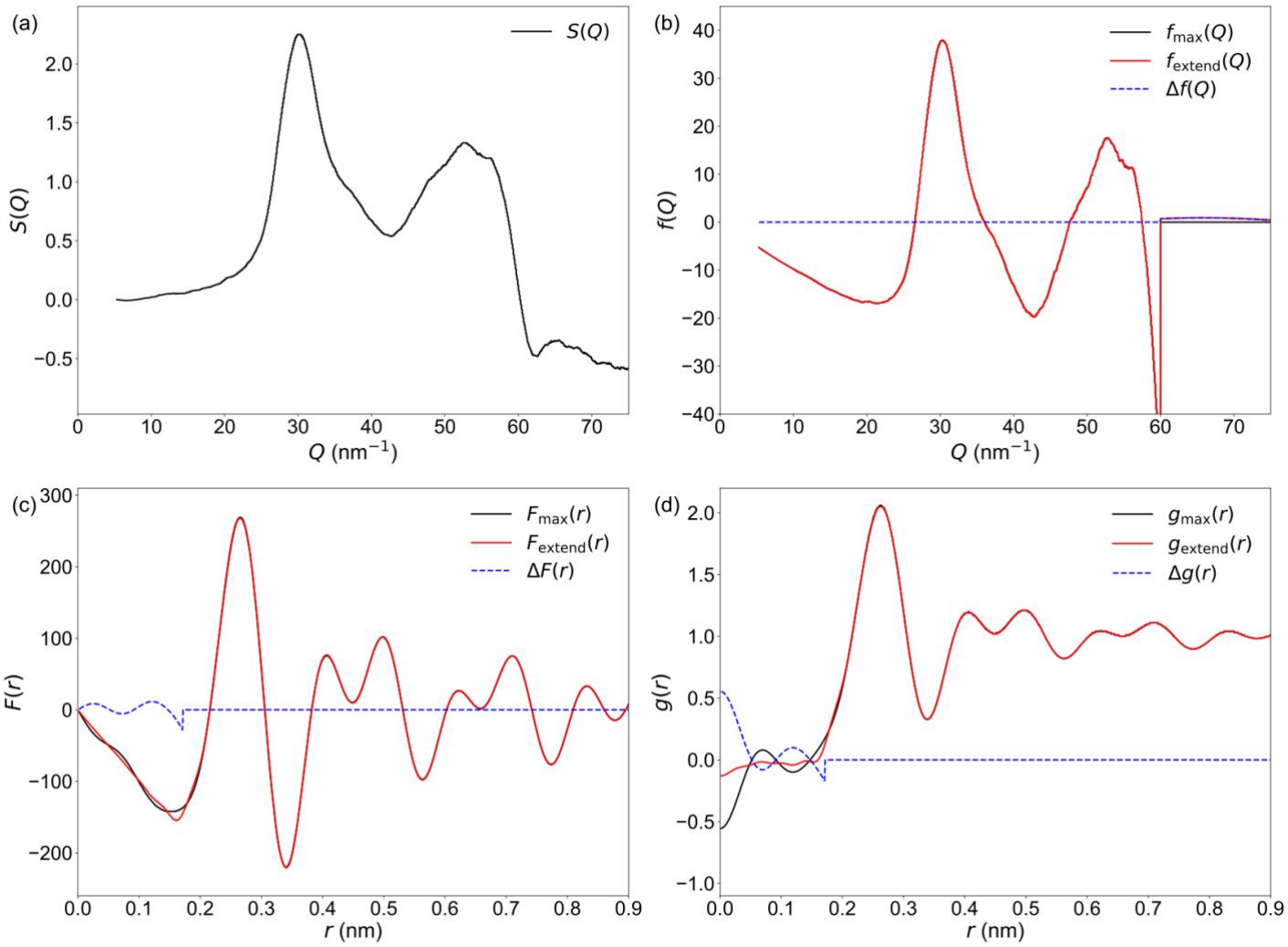

Figure S-4 Determination of liquid density from diffuse scattering using the analytical method developed by Kuwayama *et al.* (2020). **(a)** The structure factor $S(Q)$, **(b)** reduced interference function $f(Q)$, **(c)** distribution function $F(r)$, and **(d)** radial distribution function $g(r)$ (Q is momentum transfer). The black lines represent raw data, and the blue broken lines show complements added for the physical requirement that no atoms can exist at distances shorter than the nearest-neighbour atomic distance [$g(r) = 0$ at $r < r_{min}$]. With such data complements (red lines), $F(r)$ exhibits a straight line with a slope of $-4\pi\rho r$ (ρ is average atomic number density). See the supplemental text for details.

Supplementary Information References

Campbell, A.J., Danielson, L., Righter, K., Seagle, C.T., Wang, Y., Prakapenka, V.B. (2009) High pressure effects on the iron–iron oxide and nickel–nickel oxide oxygen fugacity buffers. *Earth and Planetary Science Letters* 286, 556–564. https://doi.org/10.1016/j.epsl.2009.07.022

Eggert, J.H., Weck, G., Loubeyre, P., Mezouar, M. (2002) Quantitative structure factor and density measurements of high-pressure fluids in diamond anvil cells by x-ray diffraction: argon and water. *Physical Review B* 65, 174105. https://doi.org/10.1103/PhysRevB.65.174105

Fu, S., Hirose, K., Yokoo, S., Sakai, F., Oka, K. (2025) Hydrogen in the Earth's outer core from density measurements of liquid Fe-H up to 102 GPa and 4,100 K. *Journal of Geophysical Research: Solid Earth* 130, e2025JB031934. https://doi.org/10.1029/2025JB031934

González, L.E., González, D.J. (2023) Structure and dynamics in liquid iron at high pressure and temperature: a first principles study. *Journal of Geophysical Research: Solid Earth* 128, e2022JB025119. https://doi.org/10.1029/2022JB025119

Hirao, N., Kawaguchi, S.I., Hirose, K., Shimizu, K., Ohtani, E., Ohishi, Y. (2020) New developments in high-pressure X-ray diffraction beamline for diamond anvil cell at SPring-8. *Matter and Radiation at Extremes* 5, 018403. https://doi.org/10.1063/1.5126038

Iizuka-Oku, R., Yagi, T., Gotou, H., Okuchi, T., Hattori, T., Sano-Furukawa, A. (2017) Hydrogenation of iron in the early stage of Earth's evolution. *Nature Communications* 8, 14096. https://doi.org/10.1038/ncomms14096

Ikuta, D., Ohtani, E., Sano-Furukawa, A., Shibazaki, Y., Terasaki, H., Yuan, L., Hattori, T. (2019) Interstitial hydrogen atoms in face-centered cubic iron in the Earth's core. *Scientific Reports* 9, 7108. https://doi.org/10.1038/s41598-019-43601-z

Jing, Z., Wang, Y., Kono, Y., Yu, T., Sakamaki, T., Park, C., Rivers, M.L., Sutton, S.R., Shen, G. (2014) Sound velocity of Fe–S liquids at high pressure: implications for the Moon's molten outer core. *Earth and Planetary Science Letters* 396, 78–87. https://doi.org/10.1016/j.epsl.2014.04.015

Katayama, Y., Saitoh, H., Yomogida, Y., Aoki, K. (2010) Structure of liquid iron hydrogen alloy under high pressure. *Journal of Physics: Conference Series* 215, 012080. https://doi.org/10.1088/1742-6596/215/1/012080

Kuwayama, Y., Morard, G., Nakajima, Y., Hirose, K., Baron, A.Q.R., Kawaguchi, S.I., Tsuchiya, T., Ishikawa, D., Hirao, N., Ohishi, Y. (2020) Equation of state of liquid iron under extreme conditions. *Physical Review Letters* 124, 165701. https://doi.org/10.1103/PhysRevLett.124.165701

Longhi, J. (2003) A new view of lunar ferroan anorthosites: post magma ocean petrogenesis. *Journal of Geophysical Research: Planets* 108, 5083. https://doi.org/10.1029/2002JE001941

Mita, S., Tagawa, S., Hirose, K., Ikuta, N. (2025) Fe–FeH eutectic melting curve and the estimates of Earth's core temperature and composition. *Journal of Geophysical Research: Solid Earth* 130, e2024JB029283. https://doi.org/10.1029/2024JB029283

Ohta, K., Ichimaru, K., Einaga, M., Kawaguchi, S., Shimizu, K., Matsuoka, T., Hirao, N., Ohishi, Y. (2015) Phase boundary of hot dense fluid hydrogen. *Scientific Reports* 5, 16560. https://doi.org/10.1038/srep16560

Pease, A., Liu, J., Lv, M., Piper, J., Kono, Y., Dorfman, S.M. (2025) Liquid structure of iron and iron–nitrogen–carbon alloys within the cores of small terrestrial bodies. *Journal of Geophysical Research: Planets* 130, e2024JE008599. https://doi.org/10.1029/2024JE008599

Rai, N., van Westrenen, W. (2014) Lunar core formation: new constraints from metal-silicate partitioning of siderophile elements. *Earth and Planetary Science Letters* 388, 343–352. https://doi.org/10.1016/j.epsl.2013.12.001

Seto, Y., Nishio-Hamane, D., Nagai, T., Sata, N. (2010) Development of a software suite on X-ray diffraction experiments. *The Review of High Pressure Science and Technology* 20, 269–276. https://doi.org/10.4131/jshpreview.20.269

Shibazaki, Y., Kono, Y. (2018) Effect of silicon, carbon, and sulfur on structure of liquid iron and implications for structure-property relations in liquid iron-light element alloys. *Journal of Geophysical Research: Solid Earth* 123, 4697–4706. https://doi.org/10.1029/2018JB015456

Stoutenburg, E.R., Caracas, R., Campbell, A.J. (2026) Immiscibility between hydrogen and molten iron in planetary cores. *Earth and Planetary Science Letters* 678, 119851. https://doi.org/10.1016/j.epsl.2026.119851

Tagawa, S., Sakamoto, N., Hirose, K., Yokoo, S., Hernlund, J., Ohishi, Y., Yurimoto, H. (2021) Experimental evidence for hydrogen incorporation into Earth's core. *Nature Communications* 12, 2588. https://doi.org/10.1038/s41467-021-22035-0

Tagawa, S., Helffrich, G., Hirose, K., Ohishi, Y. (2022) High-pressure melting curve of FeH: implications for eutectic melting between Fe and non-magnetic FeH. *Journal of Geophysical Research: Solid Earth* 127, e2022JB024365. https://doi.org/10.1029/2022JB024365

Tateno, S., Hirose, K., Sinmyo, R., Morard, G., Hirao, N., Ohishi, Y. (2018) Melting experiments on Fe–Si–S alloys to core pressures: Silicon in the core? *American Mineralogist* 103, 742–748. https://doi.org/10.2138/am-2018-6299

Tateno, S., Komabayashi, T., Hirose, K., Hirao, N., Ohishi, Y. (2019) Static compression of B2 KCl to 230 GPa and its *P-V-T* equation of state. *American Mineralogist* 104, 718–723. https://doi.org/10.2138/am-2019-6779

Tsujino, N., Nishihara, Y., Nakajima, Y., Takahashi, E., Funakoshi, K.-i., Higo, Y. (2013) Equation of state of γ-Fe: reference density for planetary cores. *Earth and Planetary Science Letters* 375, 244–253. https://doi.org/10.1016/j.epsl.2013.05.040

Tsutsumi, Y., Sakamoto, N., Hirose, K., Mita, S., Yokoo, S., Hsu, H., Yurimoto, H. (2025) Origin of Earth's hydrogen and carbon constrained by their core-mantle partitioning and bulk Earth abundance. *Nature Communications* 16, 10038. https://doi.org/10.1038/s41467-025-65729-5

Walker, D., Cranswick, L.M., Verma, P.K., Clark, S.M., Buhre, S. (2002) Thermal equations of state for B1 and B2 KCl. *American Mineralogist* 87, 805–812. https://doi.org/10.2138/am-2002-0701